Synthesis and Characterization of Ionic Block Copolymer Templated Calcium Phosphate Nanocomposites

M. Kanapathipillai,[#,†] Y. Yusufoglu,[#,§] A. Rawal,[‡] Y.-Y. Hu,[‡] C.-T. Lo,[||] P. Thiyagarajan,[||] Y. E. Kalay,[§] M. Akinc,[§] S. Mallapragada,[†] and K. Schmidt-Rohr*[,‡]

Ames Laboratory and Departments of Chemical Engineering, Chemistry, and Materials Engineering, Iowa State University, Ames, Iowa 50011, and Advanced Photon Source, Argonne National Laboratory, 9700 S. Cass Avenue, Argonne, Illinois 60439

Received December 4, 2007. Revised Manuscript Received April 28, 2008

Self-assembling thermo-reversibly gelling anionic and zwitterionic pentablock copolymers were used as templates for precipitation of calcium phosphate nanostructures, controlling their size and ordered structural arrangement. Calcium and phosphate ions were dissolved in a block-copolymer micellar dispersion at low temperatures. Aging at ambient temperature produced inorganic nanoparticles, presumably nucleated by ionic interactions. The self-assembled nanocomposites were characterized by small-angle X-ray and neutron scattering (SAXS/SANS), nuclear magnetic resonance (NMR), thermogravimetric analysis (TGA), and transmission electron microscopy (TEM). $^{1}H-^{31}P$ NMR with ^{1}H spin diffusion from polymer to phosphate proved the formation of nanocomposites, with inorganic particle sizes from ~2 nm, characterized by $^{1}H-^{31}P$ dipolar couplings, to >100 nm. TEM analysis showed polymer micelles surrounded by calcium phosphate. SAXS attested that a significant fraction of the calcium phosphate was templated by the polymer micelles. SANS data indicated that the order of the polymer was enhanced by the inorganic phase. The nanocomposite gels exhibited higher moduli than the neat polymer gels. The calcium phosphate was characterized by TGA, X-ray diffraction, high-resolution TEM, and various NMR techniques. An unusual crystalline phase with ≥2 chemically and ≥3 magnetically inequivalent HPO_4^{2-} ions was observed with the zwitterionic copolymer, highlighting the influence of the polymer on the calcium phosphate crystallization. The inorganic fraction of the nanocomposite was around 30 wt % of the dried hydrogel. Thus, a significant fraction of calcium phosphate has been templated by the tailored self-assembling ionic block copolymers, providing a bottom-up approach to nanocomposite synthesis.

Introduction

In most examples of successful templating of polymer−ceramic composites, the polymer−inorganic phase interaction is limited to the surface of the polymer and restricts the systematic study of the effects that variables such as ionic interaction, relative size, and concentration of polymer have on templating and nanocrystal formation.[1–4] One method to create nanocomposites and also to expand its applicability to the creation of three-dimensional macroscale structures is the dispersion of already synthesized particles or ionic solutions into the structured matrix.[4,5] But nanoparticle aggregation, high viscosity of the nanostructured materials, and incompatibility of the particle surface and ionic solutions with the polymers limit the use of these types of templating methods.[5] We have demonstrated that these problems can be circumvented by the use of self-assembling thermo-reversible block copolymer gels that can facilitate a bottom-up approach for inorganic nanocomposite synthesis.[6] Although successful templating was achieved by this approach, the percentage of inorganic precipitate in the final nanocomposite was low (~15 wt %), compared to about 70 wt % seen in nature.[7]

In the bone formation process, collagen fibrils are formed by self-assembly of collagen triple helices, and hydroxyapatite (HAp) crystals grow within these fibrils.[8] During the HAp crystal growth, acidic macromolecules such as glycoproteins that are attached to the collagen scaffold play important templating roles. Glycoproteins are covalently linked to polysaccharide side chains that often contain sulfate and carboxylate residues, and these functional groups serve as binding sites for Ca^{2+} ions.[9] To mimic natural nanocomposites better, the ionic interactions between the organic−inorganic interfaces need to be enhanced. Tanahashi et al.[10]

* Corresponding author. E-mail: srohr@iastate.edu. Phone: 515-294-6105.
[#] Both authors contributed equally to this research.
[†] Ames Laboratory and Department of Chemical Engineering, Iowa State University.
[‡] Ames Laboratory and Department of Chemistry, Iowa State University.
[§] Ames Laboratory and Department of Materials Engineering, Iowa State University.
[||] Advanced Photon Source, Argonne National Laboratory.

(1) Song, J.; Saiz, E.; Bertozzi, C. R. *J. Eur. Ceram. Soc.* **2003**, *23*, 2905–2919.
(2) Song, J.; Malathong, V.; Bertozzi, C. R. *J. Am. Chem. Soc.* **2005**, *127*, 3366–3372.
(3) Rusu, V. M.; Ng, C.-H.; Wilke, M.; Tiersch, B.; Fratzl, P.; Peter, M. G. *Biomaterials* **2005**, *26*, 5414–5426.
(4) Pozzo, D. C.; Hollabaugh, K. R.; Walker, L. M. *J. Rheol. (N.Y.)* **2005**, *49*, 759–782.
(5) Pozzo, D. C.; Walker, L. M. *Colloids Surf., A* **2007**, *294*, 117–129.
(6) Enlow, D.; Rawal, A.; Kanapathipillai, M.; Schmidt-Rohr, K.; Mallapragada, S.; Lo, C. T.; Thiyagarajan, P.; Akinc, M. *J. Mater. Chem.* **2007**, *17*, 1570–1578.
(7) Du, C.; Cui, F. Z.; Zhang, W.; Feng, Q. L.; Zhu, X. D.; De Groot, K. *J. Biomed. Mater. Res.* **2000**, *50*, 518–527.
(8) Hartgerink, J. D.; Beniash, E.; Stupp, S. I. *Science* **2001**, *294*, 1684–1688.

10.1021/cm703441n CCC: $40.75
Published on Web 08/23/2008

have shown using self-assembled monolayers that anionic polymers template better compared to cationic or nonionic polar polymers, and further, ionic blocks containing, for instance, carboxylate groups or phosphobetaines are ideal for calcium phosphate precipitation. Other studies have also indicated that carboxyl groups not only provide a site for heterogeneous nucleation of apatite but also contribute to a tight adhesion of the apatite layer to polymer films.[11] Moreover, Spanos and co-workers[12] synthesized a novel composite with 9% HAp and 91% polymer by weight made of a biocompatible synthetic polymer (sulfonated polysulfone) and HAp by the precipitation of calcium phosphate phase in aqueous suspensions of the polymer particles.

Theoretical results using molecular dynamics simulations[13] have established general conditions for successful nanotemplating methods. It has been shown, for instance, that polymers with end-group functionalized blocks with a specific affinity for the inorganic components provide a successful templating strategy.[14] In this respect, block copolymers containing blocks of sulfobetaines, which are analogues to phosphobetaines, and blocks of acrylic acids, which contain carboxylate groups, are good choices for polymer templates in biomimetic mineralization. Further, it is believed that the interactions of acrylic-acid carboxylate groups with Ca^{2+} ions mimic those of the carboxylate groups in bone.[15] Hence, many mineralization studies have focused on poly(acrylic acid)-based templates for surface mineralization studies.[15–17] However, to enable hierarchical self-assembly of nanocomposites, copolymers that can self-assemble in three dimensions at multiple length scales in the presence of the inorganic phase need to be synthesized and investigated.

As hierarchically assembling copolymer templates, we have synthesized pentablock copolymers consisting of central triblock $PEO_{100}-PPO_{65}-PEO_{100}$ Pluronic F127 copolymers modified with zwitterionic or anionic terminal blocks. The zwitterionic pentablock copolymers contain polysulfobetaine side chains, with an isoelectric point (iep) value of about 6.3. This polymer is zwitterionic over a wide range of pH $\approx 2 - 11$. The anionic pentablock copolymer, on the other hand, contains acrylic acid blocks and imparts pH sensitivity above pH ~ 6. In addition to the ionic nature, the thermoreversible ordering behavior of these polymers and their water solubility make them ideal templating materials for formation of nanocomposites. Here we study the influence

Scheme 1. Structure of the Zwitterionic Pentablock Copolymer (PentaPZ)

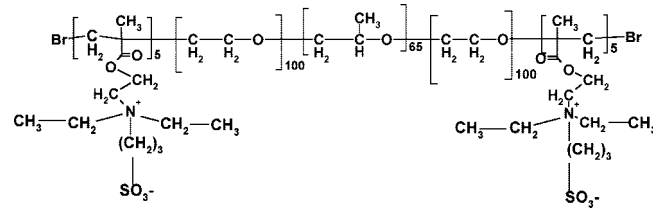

Scheme 2. Structure of the Anionic Pentablock Copolymer (PentaPAA)

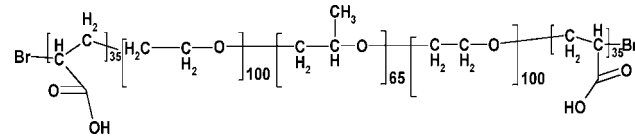

of ionic moieties of the polymer template on the formation of inorganic nanocomposites by self-assembly of thermoreversible ionic block-copolymer gel structures, a bottom-up approach that has been reported by us with cationic and Pluronic block-copolymer gels.[6] Further, along with other characterization methods, we present nuclear magnetic resonance (NMR), scattering, and electron microscopy results that support the structural picture of the polymer−inorganic nanocomposite superstructure.

Materials and Methods

All materials used were obtained from either Sigma Aldrich or Fisher Scientific and were of laboratory grade and purity.

Pentablock Copolymer Synthesis. Ionic pentablock copolymers were synthesized by atom transfer radical polymerization (ATRP). First, a cationic pentablock copolymer with poly(diethylaminoethylmethacrylate) (PDEAEM) side chains was synthesized by ATRP as described earlier.[18] This was followed by betanization of the tertiary amine groups of the side chains with propanesultone, to form the zwitterionic pentablock copolymer (PentaPZ). Its structure is shown in Scheme 1. In a typical reaction, pentablock polymer (6 g, 0.03 mmol) and 1, 3-propanesultone (30 g, 0.3 mmol) were dissolved in dry THF. The mixture was then reacted at 40 °C under argon for 2 days with continuous stirring. The reaction mixture was then precipitated with diethyl ether and vacuum-dried.

The structure of the anionic pentablock copolymer (PentaPAA) is shown in Scheme 2. For its synthesis, first the Pluronic macroinitiator was prepared as reported previously.[18] Difunctional Pluronic macroinitiator (8 g, 0.06 mmol), copper bromide (0.1885 g, 0.06 mmol), and toluene (50 mL) were added to a flask, and the solution was mixed well by stirring for 15 min. A small amount of copper was added to the reaction to enhance the stability of the Cu(I)/Cu(II) equilibrium. The flask was purged with argon for 5 min. *tert*-Butyl acrylate (2.8 g, 2.1 mmol) and N-ppm ligand (0.37 g, 0.12 mmol) were added using a syringe. The mixture was freeze-pumped/thawed three times. The reaction was then carried out at 65 °C in an oil bath overnight. The reaction mixture was then diluted in methylene chloride, passed through a short alumina column to remove the copper catalyst, and rotary-evaporated. The remaining mixture was reprecipitated in *n*-heptane and dried under vacuum. Finally, the synthesized acrylate polymer was hydrolyzed with THF and trifluoro acetic acid (TFA) (20% v/v) mixture by stirring

(9) Mann, S. *Biomineralization: Principles and Concepts in Bioinorganic Materials Chemistry*; Oxford University Press: New York, 2001; 240 pp.
(10) Tanahashi, M.; Matsuda, T. *J. Biomed. Mater. Res.* **1997**, *34*, 305–315.
(11) Miyazaki, T.; Ohtsuki, C.; Akioka, Y.; Tanihara, M.; Nakao, J.; Sakaguchi, Y.; Konagaya, S. *J. Mater. Sci.: Mater. Med.* **2003**, *14*, 569–574.
(12) Spanos, N.; Deimede, V.; Koutsoukos, P. G. *Biomaterials* **2001**, *23*, 947–953.
(13) Anderson, J. A.; Travesset, A. *Macromolecules* **2006**, *39*, 5143–5151.
(14) Knorowski, C. D.; Anderson, J. A.; Travesset, A. *Phys. Rev. Lett.* **2008**, submitted.
(15) Barbani, N.; Lazzeri, L.; Cristallini, C.; Cascone, M. G.; Polacco, G.; Pizzirani, G. *J. Appl. Polym. Sci.* **1999**, *72*, 971–976.
(16) Iwatsubo, T.; Kusumocahyo, S. P.; Kanamori, T.; Shinbo, T. *J. Appl. Polym. Sci.* **2006**, *100*, 1465–1470.
(17) Iwatsubo, T.; Sumaru, K.; Kanamori, T.; Shinbo, T.; Yamaguchi, T. *Biomacromolecules* **2006**, *7*, 95–100.
(18) Determan, M. D.; Cox, J. P.; Seifert, S.; Thiyagarajan, P.; Mallapragada, S. K. *Polymer* **2005**, *46*, 6933–6946.

overnight. The mixture was precipitated in *n*-heptane and the acrylic acid polymer was isolated after vacuum-drying.

Pentablock Copolymer Characterization. Solution NMR measurements were performed on a Varian VXR400 spectrometer, GPC measurements using PLgel columns from Polymer Laboratories, to determine the composition and molecular weights, respectively, of the block copolymers. Simple tube inversion was used to find the gelation temperature. Titration measurements were carried out using a Corning 313 pH/temperature meter at room temperature to find the pK_a and iep values, and differential scanning calorimetry (DSC) in a thermal analysis DSC instrument Q 20 was used to find the critical micellization temperatures of the copolymer solutions. Details on these measurements are given in the Supporting Information.

Pentablock−Calcium Phosphate Nanocomposite Synthesis. The calcium phosphate−polymer nanocomposite gel was synthesized using soluble calcium and phosphate salts, along the lines of the following reaction:

$$Ca(NO_3)_2 + (NH_4)_2HPO_4 + 2H_2O \rightarrow CaHPO_4{\cdot}2H_2O + 2(NH_4)NO_3 \quad (1)$$

The following procedure was used: 2.9 g of PentaPAA copolymer was mixed with 5.0 mL of 4.0 M $Ca(NO_3)_2$ in 25 mM tris-HCl solution. This solution was kept refrigerated overnight (at ~1 °C). Then 3.0 mL of 4.0 M $(NH_4)_2HPO_4$ in 25 mM tris-HCl solution was added. The polymer content of the mixture was approximately 27% by weight. The mixture was allowed to equilibrate for 1.5 days in the refrigerator. Then the sample was aged at room temperature for 2 days, resulting in a hydrogel sample at pH ≈ 5 (this sample is referred to as PentaPAA27-5). A similar procedure was followed to obtain PentaPAA36-5, where the numbers 36 and 5 again refer to wt % of the polymer and pH of the gel, respectively. For the zwitterionic PentaPZ copolymer, an organic−inorganic hydrogel with a polymer concentration of approximately 46 wt % (PentaPZ46-5) was produced in a similar fashion.

Characterization Methods. Various experiments were performed to study the structural features of the polymer-based nanocomposite. Solid-state NMR can prove nanocomposite formation and provide information regarding the size of inorganic nanoparticles as well as their composition. SAXS and SANS can determine the ordering in the gels; due to the large electron-density contrast between the organic and inorganic components, SAXS has a higher sensitivity to the structure of the inorganic phase while SANS probes mainly the structure of the polymer phase by utilizing the large contrast between ^1H and ^2H in the polymer and D_2O, respectively.[5] TEM analysis illustrates the size of the precipitated nanosize calcium phosphate particles and helps characterize them. XRD was used to identify the crystalline phases of the inorganic component. TGA measurements yielded the percentage of inorganic material in the nanocomposite. Details of the experimental parameters and the sample preparation for these techniques can be found in the Supporting Information.

Thermogravimetric analysis (TGA) was performed with a Perkin-Elmer thermogravimetric analyzer (Perkin-Elmer, TGA 7, Downers Grove, IL). Scanning transmission electron microscopy (STEM) images were captured on a JEOL 1200EX II (Japan Electron Optic Laboratories, Peabody, MA) and FEI-Tecnai G^2-F20 (FEI Inc., Hillsboro, OR) scanning transmission electron microscope equipped with an energy dispersive X-ray spectrometer EDX (EDX Inc., Mahwah, NJ). The latter instrument was also used for high-resolution TEM examination. Wide-angle X-ray diffraction patterns were obtained using a $\theta-\theta$ X-ray diffractometer (Scintag, XDS-2000, Cupertino, CA) operating at 45 kV. SAXS measurements were performed at the 12-ID beam line at the Advanced Photon Source in Argonne National Laboratory, while SANS measurements were carried out using the time-of-flight small-angle neutron diffractometer (SAND) at IPNS at Argonne National Laboratory. Solid-state NMR experiments were run using a Bruker DSX400 spectrometer (Bruker-Biospin, Rheinstetten, Germany) at 400 MHz for ^1H and 162 MHz for ^{31}P. Rheological experiments were carried out using an ARES rheometer (TA Instruments, New Castle, DE).

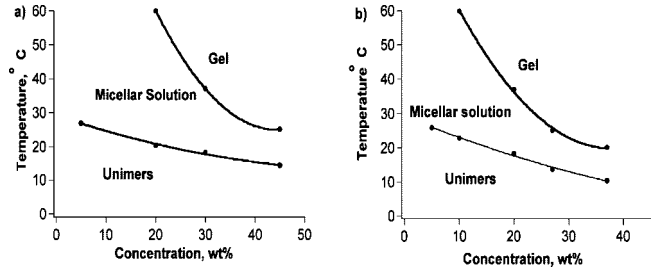

Figure 1. Phase diagrams of (a) PentaPZ (Mn, 15000), (b) PentaPAA (Mn 17538, PDI 1.196) pentablock copolymers obtained from DSC thermographs and simple gel inversion.

Results and Discussion

Polymer Characterization. The molecular weight of the cationic $PDEAEM_5-PluronicF127-PDEAEM_5$ pentablock copolymer, synthesized by ATRP, was 14570 by GPC with a narrow molecular weight distribution (PDI < 1.1). The cationic pentablock copolymer was subsequently betanized with 1,3-propanesultone in dry THF to give the PentaPZ zwitterionic polymer and the composition verified by solution NMR. The molecular weight of the PentaPAA polymer was 17538 with a narrow molecular weight distribution (PDI < 1.2).

These PentaPZ and PentaPAA copolymers exhibit micellization (see Supporting Information) and thermo-reversible gelation due to the PPO block (Figure 1 and Figure S1, Supporting Information) and impart pH-dependent solubility due to their ionic blocks. The zwitterionic pentablock copolymer exhibits pH sensitivity over a wide pH range from pH ≈ 2−11 due to the sulfobetaine blocks, with an isoelectric point around pH 6.3, where the concentrations of positive and negative charges are equal. The anionic pentablock copolymer, on the other hand, is hydrophilic above its pK_a (6.3) due to the acrylic acid side chains.

Formation of Organic−Inorganic Nanocomposites. The thermogravimetric analysis of the CaP/hydrogel samples (see Figure S2, Supporting Information) showed approximately 30 wt % inorganic for the dried hydrogels. These inorganic fractions are significantly larger than those in our previous studies of calcium phosphate formation on cationic and polar templates,[6] which yielded 6 or 15 wt % of inorganic component. The TGA results given are based on the mass of the dried hydrogel at ~200 °C as 100%.

NMR Proof of Nanocomposite Formation. Figure 2 shows ^{31}P solid-state NMR spectra (thin lines) of the PentaPAA27-5, PentaPAA36-5, and PentaPZ46-5 nanocomposites and three related model compounds. The thick lines are the corresponding spectra of the nonprotonated phosphate (PO_4^{3-}) components, obtained after recoupling of the $^{31}P\{^1H\}$ dipolar interaction for two rotation periods. Based on their chemical shifts, the peaks in Figure 2b can be tentatively assigned to brushite (large peak) and hydroxya-

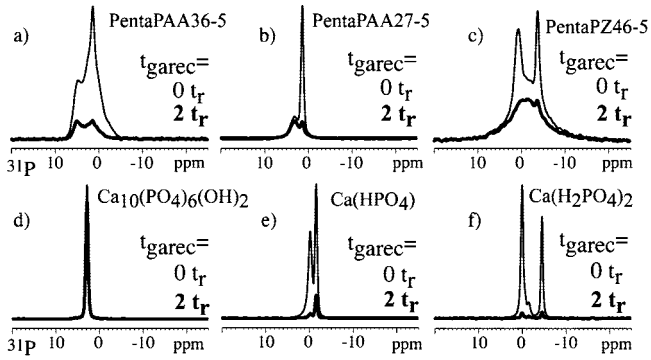

Figure 2. ^{31}P MAS NMR spectra (with direct polarization) of the synthesized polymer−calcium phosphate composites and model compounds (thin lines). Corresponding spectra with two rotation periods of $^1H-^{31}P$ recoupling are also shown (thick lines). (a) PentaPAA36-5; (b) PentaPAA27-5; (c) PentaPZ46-5; (d) hydroxyapatite; (e) monetite; (f) calcium dihydrogen phosphate. Spinning frequency: 7 kHz.

patite.[19] The spectra of the other samples contain several components that will be discussed below. The one-dimensional ^{31}P NMR spectra shown in Figure 2a−c confirm that solid phosphates are present in the samples, but do not reveal whether they are part of nanocomposites. This can be achieved instead by two-dimensional $^1H-^{31}P$ heteronuclear correlation NMR experiments with ^1H spin diffusion, where cross peaks between polymer protons and inorganic phosphate prove the intimate contact between the organic and inorganic phases that is characteristic of nanocomposites.[20,21]

Such cross peaks are not observed at short spin-diffusion times, where the phosphate "sees" only the nearest protons, i.e., those in the inorganic phase. In a nanocomposite, the polymer proton peaks appear within tens to hundreds of milliseconds of spin diffusion. The corresponding dramatic change in the heteronuclear correlation spectra are indeed observed in PentaPAA36-5; see Figure 3. Figure 3a shows contour plots of the 2D spectra for 0.05, 5, and 50 ms. Cross sections along the ^1H dimension, taken at 2.5 ppm in the ^{31}P dimension, are shown in Figure 3b. Within 50 ms, the polymer proton (OCH_2 and CH_3) peaks have become completely dominant.

The spectra of Figure 3 were acquired without homonuclear decoupling in the ^1H dimension, which makes the experiment simple to run (analogous to a WISE experiment with hypercomplex data acquisition).[22] Homonuclear decoupling is not necessary here since the high mobility of the PPO and of the parts of the PEO blocks results in sharp ^1H peaks. The application of this method to PentaPAA27-5, see Figure 3 c,d, highlights the advantage of detecting the sharp polymer peaks, even when they are small, on the background of the broader proton peaks of the inorganic phases. In this material, the polymer peaks are observed at the main 1.4 ppm ^{31}P peak only after much longer spin-diffusion times than those in PentaPAA36-5, indicating larger domain sizes

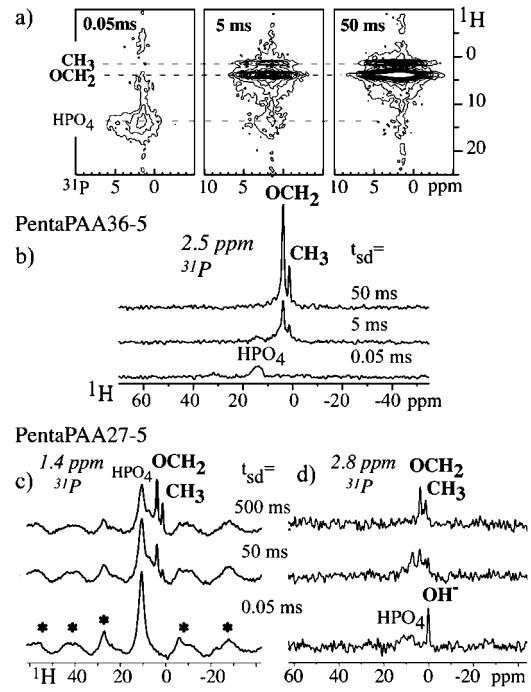

Figure 3. (a) 2D "WISE" $^1H-^{31}P$ NMR spectra of PentaPAA36-5 with spin diffusion mixing time (t_{sd}) of 0.05, 5, and 50 ms. (b) Cross sections from the 2D spectra in (a) at 2.5 ppm ^{31}P. (c, d) Cross sections from 2D "WISE" spectra of PentaPAA27-5 with spin-diffusion mixing times of 0.05, 50, and 500 ms, taken (c) at 1.4 ppm ^{31}P (spinning sidebands are marked by asterisks in the bottom trace) and (d) at 2.8 ppm ^{31}P.

of the brushite component. In contrast, Figure 3d shows that the hydroxyapatite component resonating near 2.8 ppm in the ^{31}P dimension undergoes fast spin diffusion from the polymer, within 50 ms, but its signal is weak and noisy due to relatively inefficient cross polarization of its nonprotonated PO_4^{3-} groups.

The protons with the strongest homonuclear dipolar couplings are not visible in the "WISE" spectra of Figure 3, due to their dipolar broadenings by many tens of ppm. This potential limitation is eliminated in $^1H-^{31}P$ HetCor experiments with ^1H homonuclear decoupling.[20,21] Figure 4 demonstrates how, in PentaPAA36-5, the signals of a relatively small brushite component, with strong dipolar couplings between waters of crystallization and POH protons, become visible in this version of the experiment. The sharpness of the peaks in both dimensions highlights the crystalline order of this component. In the cross section at the ^{31}P position of the brushite peak, 1.4 ppm, spin diffusion from the polymer is observed, but it is not complete within 50 ms, as witnessed by the remaining HPO_4 peak at 11 ppm still seen after 50 ms. Application of the experiment with homonuclear decoupling to PentaPZ46-5 shows only slow spin diffusion from the polymer to the ^{31}P sites with sharp peaks (see Figure S4, Supporting Information), but the low broad component centered at −1.8 ppm, which in spite of its low peak height accounts for 66% of the phosphate, exhibits close contact with the polymer.

For samples with spin-diffusion equilibration within 50 ms, a safe upper limit of 100 nm for the size of the domains can be estimated from the spin-diffusion analysis, as outlined in the Supporting Information. However, the accuracy of this approach is limited in the present systems since important

(19) Rothwell, W. P.; Waugh, J. S.; Yesinowski, J. P. *J. Am. Chem. Soc.* **1980**, *102*, 2637–2643.
(20) Hou, S. S.; Beyer, F. L.; Schmidt-Rohr, K. *Solid State Nucl. Magn. Reson.* **2002**, *22*, 110–127.
(21) Hou, S. S.; Bonagamba, T. J.; Beyer, F. L.; Madison, P. H.; Schmidt-Rohr, K. *Macromolecules* **2003**, *36*, 2769–2776.
(22) Schmidt-Rohr, K. *Macromolecules* **1992**, *25*, 3273–3277.

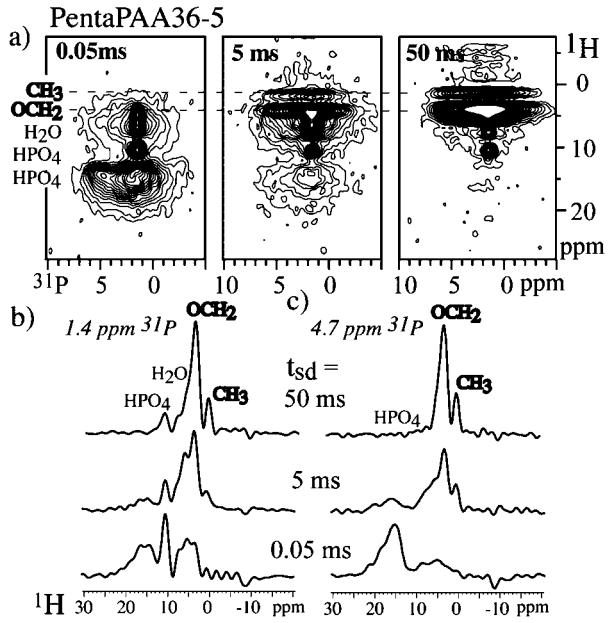

Figure 4. (a) Series of 2D ^{1}H−^{31}P HETCOR NMR spectra of PentaPAA36-5 with spin-diffusion mixing times of 0.05, 5, and 50 ms. (b) and (c) are cross sections of the 2D spectra at 1.4 and 4.7 ppm ^{31}P, revealing different ^{1}H environments.

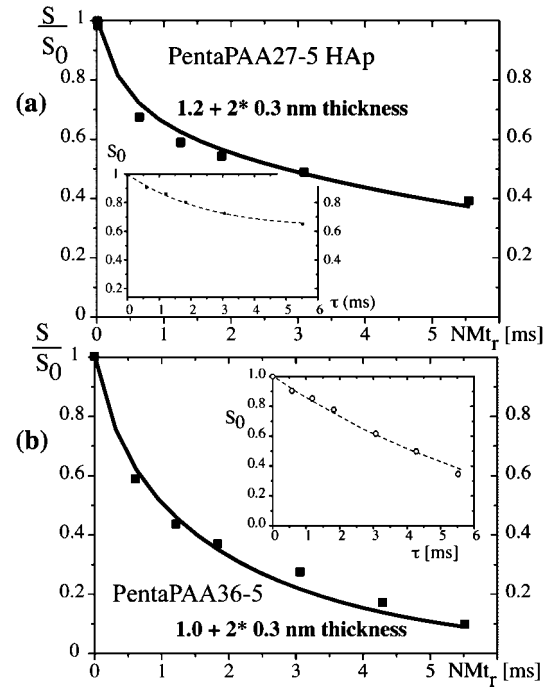

Figure 5. ^{31}P{^{1}H} HARDSHIP NMR dephasing of (a) PentaPAA27-5 at 2.8 ppm ^{31}P and (b) PentaPAA36-5 at 4.5 ppm ^{31}P. Recycle delay: 100 s. Spinning frequency: 13 kHz. $Mt_r = 0.15$ ms. The inset shows the S_0 decay under ^{1}H decoupling.

parameters, such as the diffusion coefficients, are not known with sufficient accuracy or are difficult to include in spin-diffusion simulations, such as different proton densities in the organic and inorganic components. Quantifying the thickness of the smaller inorganic particles by ^{31}P{^{1}H} HARDSHIP NMR and the supramolecular structure by SAXS, with component fractions and domain-size estimates from NMR, is a more promising approach, taken below.

Domain Thickness from ^{31}P{^{1}H}HARDSHIP NMR. The ^{1}H spin-diffusion method requires that there are protons within the inorganic phase, at a significant concentration. If that is not the case, for instance in hydroxyapatite, we can use a complementary method based on the strongly distance-dependent dipolar couplings between ^{31}P in the nanoparticles and ^{1}H in the polymer matrix. The couplings of ^{31}P to dispersed protons within the inorganic phase, which would interfere with this approach if simple ^{31}P{^{1}H} REDOR[23] was used, are refocused in the recently introduced ^{31}P{^{1}H} HARDSHIP method. [24] The HARDSHIP dephasing curve reflects the surface-to-volume ratio of the inorganic phase, with an accuracy that is significantly greater than that of ^{1}H spin diffusion in nanocomposites. ^{31}P{^{1}H} HARDSHIP dephasing in plates of 4 nm thickness or spheres of 12 nm diameter can be observed quite easily.[24]

Figure 5a shows ^{31}P{^{1}H} HARDSHIP dephasing of hydroxyapatite in PentaPAA27-5 measured at 13 kHz MAS with the optimum HARDSHIP pulse sequence.[24] The dephasing can be fit by assuming layers of 1.8 nm thickness or spheres of 6 nm diameter. The dephasing of the major component in PentaPAA36-5, Figure 5b, yields a similar result but with a larger uncertainty due to the relatively short T_{2H} of the protons within the inorganic component, which requires a significant correction of the simulation curves at longer recoupling times.[24] Experiments on brushite, $CaHPO_4 \cdot 2H_2O$, showed that due to its high proton density, the homonuclear dipolar couplings are too strong and the T_{2H} is too short for HARDSHIP to work well.

SAXS and SANS: Evidence of Templating. SAXS and SANS provide direct information on the morphology and ordering of structures in the gels and nanocomposites. In SANS, the contrast is due to the nuclear scattering length difference between the D_2O and the polymer/inorganic phase. As shown in Figure 6a, the self-assembled zwitterionic PentaPZ46-5 copolymer gels both with and without calcium phosphate display distinct first-order diffraction peaks in SANS data. The second-order peak position in relation to the first-order peak (Q^*) in the neat polymer gel clearly indicates hexagonal close packing of cylinders in the ordering of micelles. However, in the case of the nanocomposite gel, the first-order diffraction peak broadens, making the second-order peak less visible, presumably due to disorder introduced by the templating of calcium phosphate on the polymer phase.

The SAXS data in Figure 6b show similar diffraction peaks both without and with calcium phosphate. The peak intensity is greatly increased in the composite, which proves that a significant fraction of the high-electron density inorganic phase is templated by the block copolymer micelles and thus enhances their structure factor. The diffraction peaks are observed at Q/Q^* values of 1, $\sqrt{3}$, $\sqrt{7}$, and $\sqrt{12}$, indicating hexagonal close packing of rodlike polymer micelles consistent with the SANS data. With use of the Q^* value for the gels with cylinder phase the lattice spacing $d = (4/3)^{1/2}(2\pi/Q^*)$ can be determined. Furthermore, in the low

(23) Gullion, T.; Schaefer, J. *JMR* **1989**, *81*, 196–200.
(24) Schmidt-Rohr, K.; Rawal, A.; Fang, X. W. *J. Phys. Chem.* **2007**, *126*, 054701.

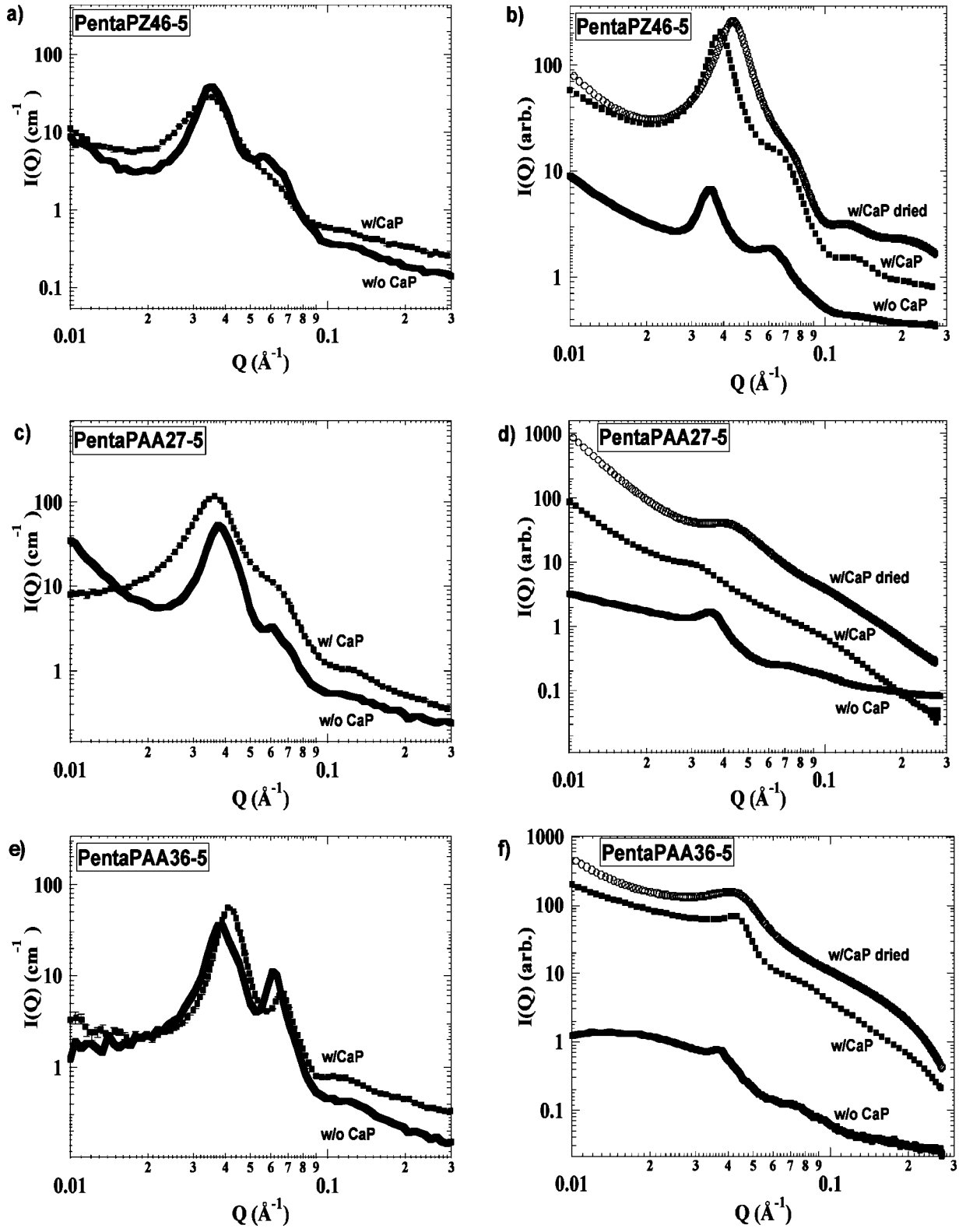

Figure 6. SANS and SAXS data of the three nanocomposites: (a) SANS and (b) SAXS of PentaPZ46-5 polymer− inorganic nanocomposite gels at pH 5.0; (c) SANS and (d) SAXS of PentaPAA27-5 polymer nanocomposite gels; (e) SANS and (f) SAXS of PentaPAA36-5 polymer−inorganic nanocomposite gels.

Q region of the SAXS data the scattering intensity $I(Q)$ varies as $Q^{-1.5}$, suggesting that both the neat and the nanocomposite gels have rodlike structures, in agreement with the TEM data below.

The lattice spacings (the characteristic distance between the centers of the cylinders) from the SANS data of the neat and the calcium phosphate templated PentaPZ46-5 polymer gels were around 18.5 nm, indicating little effect of the inorganic component on the superstructure. This may be due to the relatively small inorganic volume fraction in the nanocomposite. Similar trends were observed in the SANS data for PentaPAA27-5 (Figures 6 c,d) and PentaPAA36-5

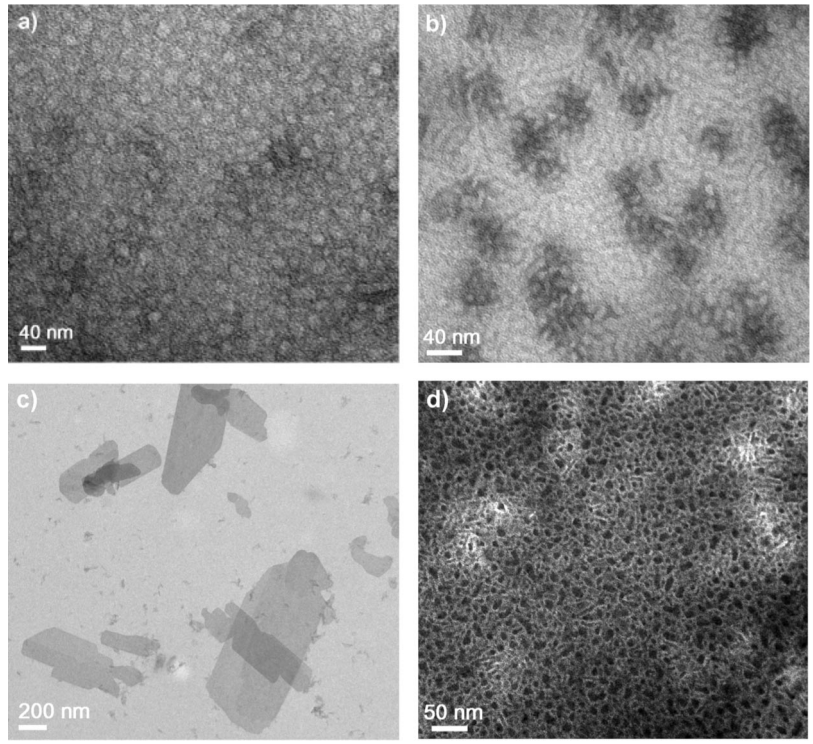

Figure 7. Transmission electron micrographs of stained (a) 5 wt % PentaPAA polymer prepared in deionized water, (b) PentaPAA36-5 nanocomposite deposited from a suspension diluted to 5 wt % polymer, (c) crystallites collected from the bottom of the vial containing the diluted PentaPAA36-5 material, and (d) high-angle annular dark field (HAADF) image of PentaPAA27-5 sample. Dark spots: polymer.

(Figure 6 e,f) polymer−gel nanocomposites. However, in contrast to the PentaPZ46-5 gels, the PentaPAA gels exhibit sharper peaks in the SANS patterns, indicating a higher level of ordering. Further, the PentaPAA36-5 neat polymer shows diffraction peaks at Q/Q^* values of 1, $\sqrt{3}$, 2, and $\sqrt{8}$, indicating FCC packing of spherical polymer micelles consistent with the SAXS and TEM data. With use of the Q^* value for gels with FCC structure, the lattice spacing $d = 2\pi/Q^*$ can be determined. The d-spacings in the gel structures of PentaPAA27-5 and PentaPAA36-5 are around 16 nm, but there was a slight reduction in the d-spacing in the presence of calcium phosphate when compared to the neat polymers. In the case of PentaPAA27-5 the polymer phase has ionic character and the broadening of the peak in the SANS pattern for the neat polymer gel might be due to electrostatic repulsion between the micelles, leading to a looser packing of particles. The sharper peaks in the presence of calcium phosphate might be due to charge neutralization in the PentaPAA gels, leading to more ordered dense packing.

The SAXS data show relatively low intensity for the neat PentaPAA polymer gels due to low X-ray contrast between polymer and water. In the presence of the inorganic component, much higher scattering intensity was again observed for PentaPAA36-5 with a scattering peak corresponding to a d-spacing of ∼15 nm, proving templating of calcium phosphate on the polymer micelles. Furthermore, the SAXS curves of both PentaPAA nanocomposites show power-law scattering with a higher exponent (∼4) in the low Q region. This suggests the presence of larger inorganic aggregates with 3-dimensional morphology. The higher power-law exponent in the case of PentaPAA27-5 when compared to PentaPAA36-5 suggests the presence of larger calcium phosphate aggregates in the former, in agreement with the NMR data. It is interesting to note that the small-angle upturn in the SAXS curves could be attributed not just to larger inorganic particles but alternatively to a superstructure of the mineralized micelles, such as 0.2 μm diameter aggregates. The TEM data show that larger inorganic particles are indeed present. The dried nanocomposite gel sample exhibits SAXS patterns similar to those of the gel samples. However, a small shift in the scattering patterns toward larger Q-values (smaller spacings) was observed, which is expected due to the removal of water.

TEM. Transmission electron micrographs of 5 wt % PentaPAA and PentaPZ polymers prepared by diluting the neat gels in deionized water (Figures 7a and 8a) revealed approximately 15 nm diameter spheroidal micelles, in agreement with the SAXS and SANS results and our previous studies.[6] Figure 7b shows a TEM image of PentaPAA36-5 nanocomposite gel diluted to 5 wt % polymer. According to STEM-EDX measurements, both calcium and phosphate (dark regions in Figure 7b) are present around the micelles. Further images are shown in Figure S6 of the Supporting Information. The atomic ratio of calcium to phosphorus for PentaPAA27-5 was found to be about 1, quite close to that of brushite (Ca/P = 1) and in agreement with XRD and NMR. For PentaPAA36-5, in addition to regions with Ca/P = 1, some areas with a Ca/P ratio of 1.9 were also observed, indicating that there is another calcium phosphate phase other than brushite, consistent with NMR. Further, Figure 7c shows a TEM micrograph of platelike calcium phosphate crystallites collected from the bottom of the redissolved polymer in PentaPAA36-5, consistent with

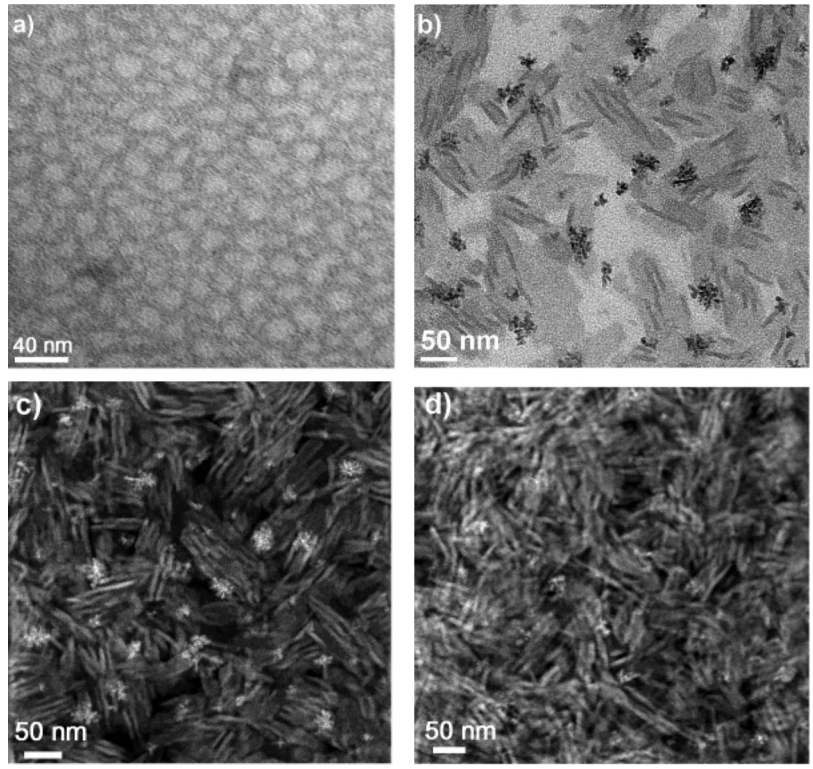

Figure 8. Transmission electron micrographs of stained (a) 5 wt % PentaPZ polymer prepared in deionized water, (b) PentaPZ46-5 nanocomposite deposited from a suspension diluted to 5 wt % polymer, and (c, d) HAADF images of the same sample.

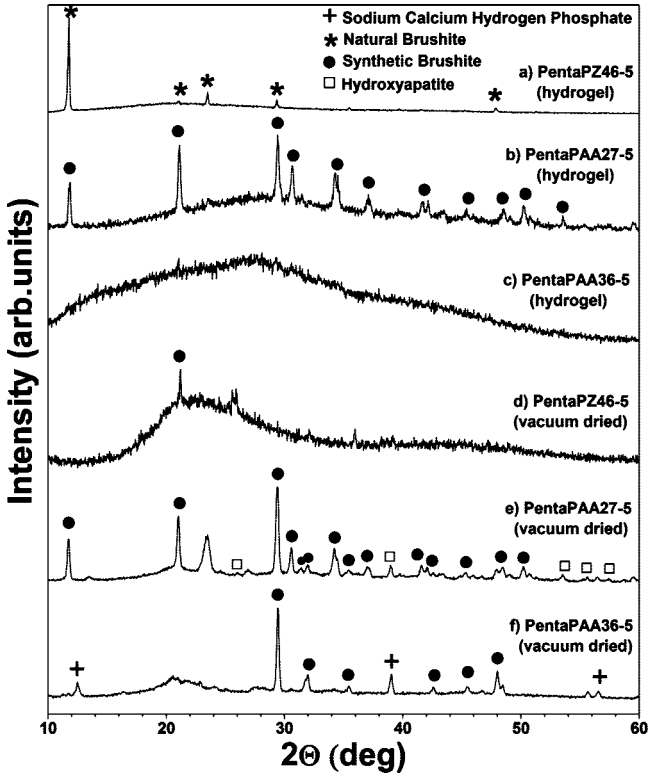

Figure 9. X-ray diffraction patterns of as-prepared hydrogel/calcium phosphate nanocomposites and vacuum-dried PentaPZ46-5, PentaPAA27-5, and PentaPAA36-5.

the larger calcium phosphate particles inferred from spin-diffusion NMR. The inorganic coating of some of the micelles can be seen more clearly in Figure 7d, which displays a high-angle annular dark field (HAADF) image of PentaPAA27−5.

Figure 8 illustrates TEM micrographs of PentaPZ polymer and PentaPZ46-5 nanocomposite. The neat polymer (5 wt % in deionized water) revealed the typical ∼15 nm diameter spherical micelles (Figure 8a). By contrast, the morphology observed for the PentaPZ46-5 nanocomposite is quite different (see Figures 8 b−d), exhibiting rodlike calcium phosphate nanoparticles. The presence of Ca and P was confirmed by STEM-EDX and the atomic Ca/P ratio was found to be around 1.0 for PentaPZ46-5.

XRD Analysis. Figure 9 shows the X-ray diffraction patterns of the hydrogel and vacuum-dried hydrogel samples, respectively. As seen from Figure 9b, the X-ray diffraction pattern of PentaPAA27-5 revealed the typical reflections for crystalline synthetic brushite ($CaHPO_4 \cdot 2H_2O$) (ICDD card #09-0077). XRD of PentaPAA36-5 showed only broad reflections, indicating that the calcium phosphate phase might be amorphous, nanocrystalline, or a minor volume fraction compared to the polymer (Figure 9c). Moreover, the characteristic peaks of natural brushite (ICDD card #11-0293), a mineral previously found mostly in caves,[25] were observed for PentaPZ46-5, shown in Figure 9a, and this is similar to our previous results with PDEAEM-modified Pluronic F127 pentablock gel composite as templates.[6]

After vacuum-drying of the hydrogel samples, the natural brushite peaks disappeared for PentaPZ46-5, while weak HAp peaks appeared in addition to synthetic brushite peaks for PentaPAA27-5 (Figure 9d and 9e), in agreement with NMR. Further, sharp peaks of brushite and sodium calcium hydrogen phosphate were observed for PentaPAA36-5 after

(25) Murray, J. W.; Dietrich, R. V. *Am. Mineral.* **1956**, *41*, 616–626.

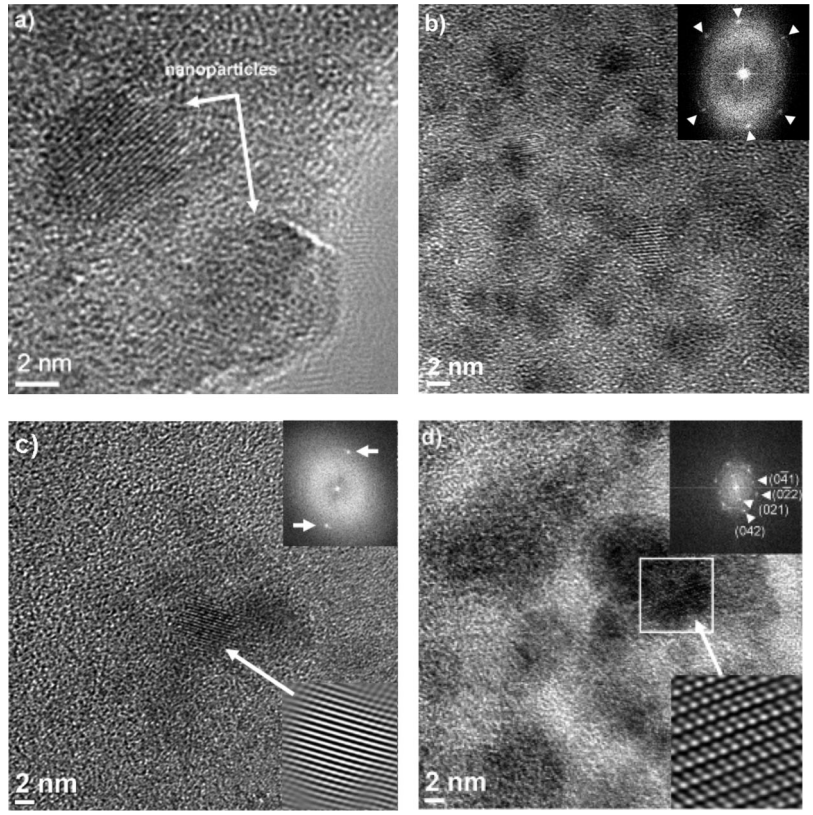

Figure 10. HRTEM images of (a, b) PentaPAA36-5, (c) PentaPZ46-5, and (d) PentaPAA27-5. The upper and lower insets show the FFT patterns and filtered inverse-FFT images, respectively. While nanocrystalline brushite was determined to be present in PentaPAA36-5, the type of calcium phosphate phase was not identified with certainty for PentaPZ46-5. The existence of brushite in PentaPAA27-5 was confirmed from the analysis of Figure 10d.

drying (Figure 9f). With use of the Scherrer equation, brushite crystal sizes of >40 nm and >45 nm were estimated from the widths of the Bragg peaks for the vacuum-dried PentaPAA36-5 and PentaPAA27-5, respectively.

HRTEM. The characteristics of the crystalline calcium phosphate phases in the hydrogel samples were investigated using high-resolution transmission electron microscopy (HR-TEM), as shown in Figure 10. Nanocrystalline particles within the amorphous polymer matrix are clearly seen from the HRTEM images (marked by arrows in parts (a), (c), and (d) of Figure 10). The insets in Figure 10b−d show fast Fourier transform (FFT) patterns of the full area of the HRTEM images. Arrows on the FFT pattern indicate the diffracted intensity from the nanocrystals within the amorphous polymer matrix. The measured lattice spacing for PentaPAA36-5 in Figure 10b is in good agreement with the distance between (041) planes in synthetic brushite (compared with ICDD card #09-0077), consistent with XRD and NMR of PentaPAA36-5. Figure 10c presents a HRTEM image of PentaPZ46-5 and the lower inset in Figure 10c shows the filtered inverse-FFT image of an isolated nanocrystal, calculated by masking all but the spots shown by the arrows in the FFT pattern. Although the existence of crystalline phases in the diluted PentaPZ46-5 hydrogel was confirmed by HRTEM, these nanocrystals could not be identified as one of the calcium phosphate phases with certainty since the measured lattice spacings did not show any characteristic low index planes. The HRTEM micrograph in Figure 10d confirms the existence of nanocrystalline brushite in PentaPAA27-5, in agreement with XRD and

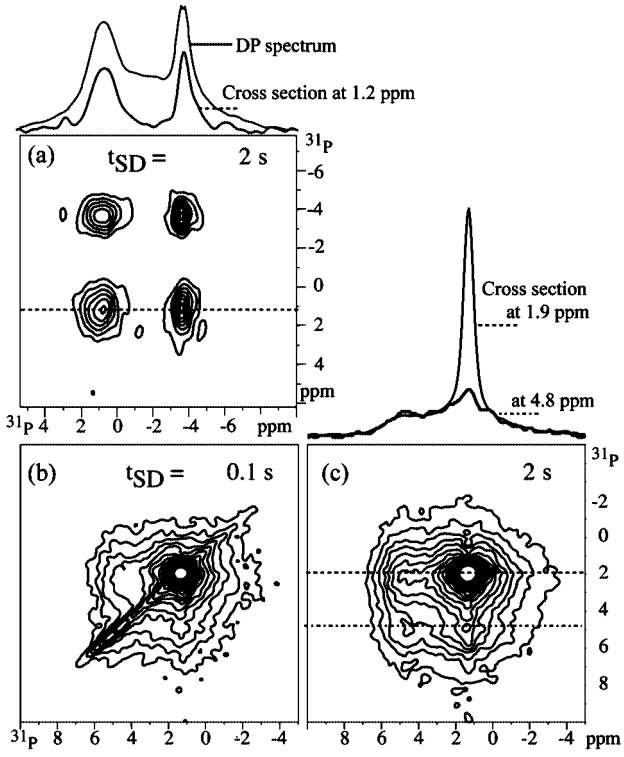

Figure 11. ^{31}P two-dimensional exchange NMR spectra of (a) PentaPZ46-5, mixing time 2 s; (b) PentaPAA36-5, mixing time 100 ms, (c) PentaPAA36-5, mixing time 2 s. Spinning frequency: 6.5 kHz. The 1D spectra shown on top of (a) are the regular DP ^{31}P MAS spectrum and a cross section from the 2D exchange spectra at 1.2 ppm ^{31}P as indicated. The 1D spectra on top of (c) are cross sections from the data set of PentaPAA36-5 at 1.9 and 4.8 ppm ^{31}P as indicated.

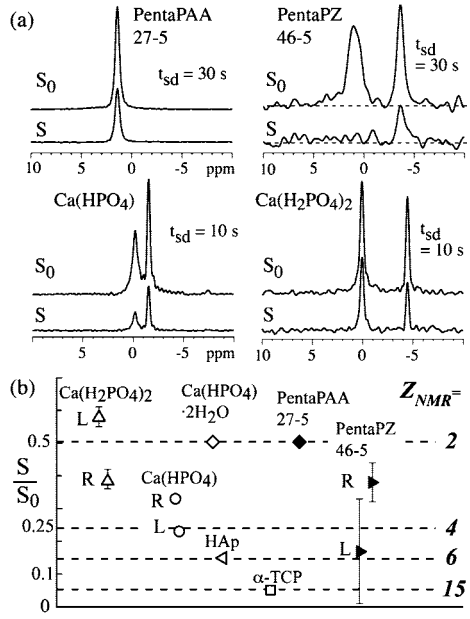

Figure 12. Determination of the number of magnetically inequivalent sites in the crystalline calcium phosphates by ^{31}P CODEX NMR with 10 or 30 s of ^{31}P spin diffusion. (a) Spectra after spin exchange (S) compared with reference spectra (S_0). (b) Plot of S/S_0 for the three nanocomposites and several model compounds. L: left peak; R: right peak.

NMR. The FFT pattern of the nanocrystal shown in the upper inset agrees well with the [100] zone axis of brushite.

The size of the nanocrystals detected by HRTEM is on the order of 5−10 nm, which is smaller than the value estimated from XRD. However, it should be noted that HRTEM samples a very small volume of the specimen compared to XRD and NMR techniques. Moreover, HRTEM requires a specimen thickness of <50 nm and features contained within the field of view. Therefore, the probability of imaging smaller-than-average nanocrystals is high in HRTEM observations.

NMR Characterization of Calcium Phosphates. Based on ^{31}P NMR peak positions[19,26] and phosphate protonation (Figure 2), the ^{31}P spectrum of PentaPAA27-5 can be assigned to brushite (large peak at 1.4 ppm) and hydroxyapatite (broader band at 2.8 ppm). The assignment is confirmed by the proton peak positions in their ^{1}H−^{31}P spectra without spin diffusion (bottom traces in Figure 3 c,d): The OH^- proton of HAp is detected near 0.5 ppm, while the relatively sharp signals near 11 ppm agrees with that of HPO_4 in brushite from the literature. [27] In ^{1}H−^{31}P HetCor spectra with homonuclear decoupling, the 6.5 ppm ^{1}H signal of waters of crystallization in brushite[27] is also detected. This is fully consistent with the XRD analysis of this sample; see Figure 9. Deconvolution of the ^{31}P NMR signal yields a brushite:HAp phosphate ratio of 71:29, with a 5% disordered component accounted in the 71% brushite.

The NMR analysis of the two other samples is not so straightforward. Therefore, we have identified further observables, such as the protonation of the phosphates and the number of inequivalent phosphates in the asymmetric unit cell.

HPO_4 versus PO_4 Ions. Protonation of the phosphate ions was probed by NMR using simple ^{31}P{^{1}H} gated decoupling with recoupling for a maximum of two rotation periods. Figure 2 compares spectra after 0 (thin line) and $2t_r$ (thick line) of ^{31}P{^{1}H} recoupling, while Figure S5 in the Supporting Information shows a plot of the peak intensity as a function of recoupling time. The fast signal decay of the sharp peaks in parts (a) and (c) of Figure 2 shows that a large fraction of phosphates in PentaPAA36-5 and PentaPZ46-5 are protonated (HPO_4^{2-}). Much slower dephasing is observed in Figure 2b, g for the 2.8 ppm signal in PentaPAA27-5, confirming its assignment to hydroxyapatite, and for the broad peak in PentaPZ46-5 centered at −1.5 ppm. The broad signal of PentaPAA36-5 decays with an intermediate rate. The dephasing thus also provides for spectral editing of overlapping signals in all three nanocomposite samples; see Figure 2a−c.

Number of Inequivalent Sites from NMR. The spectra of PentaPAA36-5 and PentaPZ46-5 show multiple peaks or shoulders, which might arise from different phases or from different sites in the unit cell of one phase. To distinguish between these two situations, we performed ^{31}P 2D exchange experiments with ^{31}P spin diffusion in the mixing time of 2 s, which allows for equilibration on the 2 nm scale. Figure 11a shows such a 2D spectrum for PentaPZ46-5. Pronounced cross peaks between the two relatively sharp resonances prove that they belong to sites within one unit cell. The larger area of the left peak and its circular diagonal peak after spin diffusion suggests that these are actually two unresolved peaks, giving a total of three chemically inequivalent sites. The broad band centered on −2 ppm in the DP spectrum (top trace above Figure 11a) is not observed in this 2D spectrum due to its short ^{31}P T_1 relaxation time of less than 2 s. The different T_1 relaxation times in themselves prove that the ^{31}P associated with the broad band and the two sharp peaks are not within spin-diffusion contact, i.e., not in the same phase.

^{31}P 2D exchange spectra of PentaPAA36-5 are shown in Figure 11 b,c. After a spin-diffusion time of 0.1 s, Figure 11b, a diagonal ridge is still visible because the magnetization has not yet equilibrated locally. The ridge has disappeared after 2 s, and ^{31}P spin diffusion between the broad bands with maxima near 1.2 and 4.8 ppm is observed. The difference in the two cross sections displayed above Figure 11c shows that the sharp peak at 1.9 ppm corresponds to a phase (crystalline brushite) separate from the major component producing the broad double-peaked intensity.

The number of orientationally inequivalent sites can be estimated by ^{31}P CODEX NMR with ^{31}P spin diffusion. In this experiment, a stimulated echo is detected under magic-angle spinning with recoupling of the chemical-shift anisotropy before and after a mixing time for spin diffusion. For sufficiently long dephasing/rephasing and mixing times, only magnetization remaining on the original ^{31}P site, or on magnetically equivalent sites, contributes to the stimulated echo. In a crystal with Z inequivalent sites in the asymmetric

(26) Kolodziejski, W. *Top. Curr. Chem.* **2004**, *246*, 235–270.
(27) Yesinowski, J. P.; Eckert, H. *J. Am. Chem. Soc.* **1987**, *109*, 6274–6282.

Table 1. Parameters of the Synthesized Materials from Solid-State NMR Results and the Corresponding NMR Methods Used

	NMR method				
sample	inorganic fractions (^{31}P DP) ± 3%		inorganic protons and their concentration (WISE & HETCOR)	inequiv. phosphates in unit cell (CODEX)	thickness d (WISE, HETCOR & HARDSHIP)
PentaPAA 36-5	partly disordered	88%	sparse HPO_4 low conc.	unknown	$d = 1.6$ nm
	brushite $(HPO_4)^{2-}$	12%	HPO_4 and H_2O high conc.	2	$d \geq 20$ nm
PentaPAA 27-5	HAp $(PO_4)^{3-}$	29%	OH^-, H_2O, and HPO_4 low conc.	6	$d = 1.8$ nm
	brushite $(HPO_4)^{2-}$	71%	HPO_4 and H_2O high conc.	2	50 nm $< d <$ 1 μm
PentaPZ 46-5	disordered $(PO_4)^{3-}$	66%	H_2O low conc.	N/A	$d <$ 20 nm
	crystalline $(HPO_4)^{2-}$	34%	H_2O and HPO_4 high conc.	3 or 4	50 nm $< d <$ 1 μm

unit cell, the signal thus decays from 1 to 1/Z.[28] Figure 12 compares the long-time with the full initial intensity for the three nanocomposites and three model calcium phosphates. The normalized final intensities S/S_0 are plotted in Figure 12 b. For the model compounds, they mostly match the 1/Z values expected from the known crystal structures. The 1/Z values for PentaPZ46-5 between 1/3 and 1/4 are significantly lower than those for $Ca(H_2PO_4)_2$, confirming that these are different crystal structures in spite of their relatively similar 1D spectra.

Synopsis of Structural Findings. Table 1 summarizes the results of the composition and other properties of the inorganic components of the nanocomposites obtained from NMR and XRD.

PentaPAA36-5 contains crystalline brushite and a partially disordered phosphate component at a molar ratio of 12:88. The latter has particles of <2 nm thickness in close proximity with the polymer micelles, while the brushite crystallites are larger.

PentaPAA27-5 contains brushite and hydroxyapatite at a phosphate molar ratio of 71:29, as clearly shown by XRD and various NMR experiments. A 5% disordered HPO_4^{2-} component is accounted in the 71% brushite; it might be a surface layer of the nanocrystals. The hydroxyapatite forms a ~1.8 nm thick crystalline partial coating of the polymer micelles, while the brushite is present as larger nanocrystals. While we have found that neat brushite quickly converts into the more stable, dehydrated monetite, the brushite in the nanocomposite appears to be stabilized.

PentaPZ46-5 contains amorphous PO_4^{3-} and crystalline HPO_4^{2-} phosphates at a 66:34 ratio, which have been separated spectroscopically based on their different rates of dephasing in gated decoupling and in ^{31}P T_1 relaxation experiments (Figures 2c and 11a). The majority amorphous component has been templated by the polymer micelles, while the crystalline component forms crystallites of >50 nm width. The crystalline calcium phosphate contains at least two, probably three chemically inequivalent and at least three magnetically inequivalent HPO_4^{2-} ions, but it has not been assigned to a specific modification yet; it is not a sodium calcium phosphate since the sodium concentration in this sample (PentaPZ46-5) is particularly low. XRD does not show many distinctive peaks to help with the assignment. It is reasonable to propose that this unusual phosphate phase has been nucleated by the zwitterionic polymer, highlighting the influence of the polymer end block on the calcium phosphate crystallization.

Acknowledgment. This work was supported by the U.S. Department of Energy under Contract DE-AC02-07CH11358. This work benefited from the use of IPNS and APS, funded by the U.S. DOE, Office of Science, Office of Basic Energy Science, under Contract DE-AC02-06CH11357. We wish to thank Matthew J. Kramer for helpful discussion of the TEM results.

Supporting Information Available: Details on the experimental techniques and associated sample preparation, further materials characterization, and additional NMR as well as TEM data (PDF). This information is available free of charge via the Internet at http://pubs.acs.org.

CM703441N

(28) Reichert, D.; Bonagamba, T. J.; Schmidt-Rohr, K. *J. Magn. Reson.* **2001**, *151*, 129–135.